LA-UR-15-20916 (Accepted Manuscript)

Comparative Response of Microchannel Plate and Channel Electron Multiplier Detectors to Penetrating Radiation in Space

Funsten, Herbert O.

Provided by the author(s) and the Los Alamos National Laboratory (2016-09-20).

To be published in: IEEE Transactions on Nuclear Science

DOI to publisher's version: 10.1109/TNS.2015.2464174

Permalink to record: http://permalink.lanl.gov/object/view?what=info:lanl-repo/lareport/LA-UR-15-20916

Disclaimer:
Approved for public release. Los Alamos National Laboratory, an affirmative action/equal opportunity employer, is operated by the Los Alamos National Security, LLC for the National Nuclear Security Administration of the U.S. Department of Energy under contract DE-AC52-06NA25396. Los Alamos National Laboratory strongly supports academic freedom and a researcher's right to publish; as an institution, however, the Laboratory does not endorse the viewpoint of a publication or guarantee its technical correctness.

Comparative Response of Microchannel Plate and Channel Electron Multiplier Detectors to Penetrating Radiation in Space

Herbert O. Funsten, *Member, IEEE*, Ronnie W. Harper, Eric E. Dors, Paul A. Janzen, Brian A. Larsen, Elizabeth A. MacDonald, David I. Poston, Stephen M. Ritzau, Ruth M. Skoug, and Thomas H. Zurbuchen

***Abstract*—Channel electron multiplier (CEM) and microchannel plate (MCP) detectors are routinely used in space instrumentation for measurement of space plasmas. Our goal is to understand the relative sensitivities of these detectors to penetrating radiation in space, which can generate background counts and shorten detector lifetime. We use 662 keV γ-rays as a proxy for penetrating radiation such as γ-rays, cosmic rays, and high-energy electrons and protons that are ubiquitous in the space environment. We find that MCP detectors are $\sim$ 20 times more sensitive to 662 keV γ-rays than CEM detectors. This is attributed to the larger total area of multiplication channels in an MCP detector that is sensitive to electronic excitation and ionization resulting from the interaction of penetrating radiation with the detector material. In contrast to the CEM detector, whose quantum efficiency ε_γ for 662 keV γ-rays is found to be 0.00175 and largely independent of detector bias, the quantum efficiency of the MCP detector is strongly dependent on the detector bias, with a power law index of 5.5. Background counts in MCP detectors from penetrating radiation can be reduced using MCP geometries with higher pitch and smaller channel diameter.**

***Index Terms*—Electron multipliers, gamma-ray effects, plasma measurements, radiation effects.**

I. Introduction

ELECTRON multiplier detectors such as microchannel plate (MCP) and channel electron multiplier (CEM) detectors are used extensively in space-based instruments for many applications, such as detection of photons [1], [2], plasma spectrometry [3]–[5], and energetic neutral atom imaging [6]–[8]. These incident particles are easily converted to low energy secondary electrons or photoelectrons, which initiate an electron avalanche in both MCP and CEM detectors. The resulting electron pulse is registered as a count in the instrument. We present the results of an experiment in which we compare the response of MCP and CEM detectors to 662 keV γ-rays, which serve as a proxy for penetrating radiation.

In the space environment, CEM and MCP detectors are also sensitive to penetrating radiation that produces low energy electrons that can likewise initiate an electron avalanche and register a background count [9]. Penetrating radiation can include γ-rays, neutrons, electrons greater than $\sim$ 10 MeV, and ions greater than $\sim$ 100 MeV.[1] In the space environment, sources of these background particles can come (a) from natural systems such as planetary radiation belts, the Sun, and cosmic rays; (b) from engineered systems such as radioisotope thermoelectric generator (RTG) power sources, and (c) as spallation products generated by the interaction of energetic particles with the spacecraft.

As an example, Fig. 1 shows electron count rate as a function of time and energy passband from the ACE/SWEPAM-E solar wind electron spectrometer [3]. At day $\sim$ 308.7 in 2001, the onset of a solar energetic particle (SEP) event is noted in the sudden rise in the count rates of higher energy electrons. Before this event, the electron count rates span a factor of $\sim 10^3$, from $\sim$ 70 cts per spin at 1.3 keV to $\sim 7 \times 10^4$ cts per spin at 73 eV, which is typical for the undisturbed solar wind. After onset of the SEP, which is primarily protons and heavy ions up to several hundred MeV [11], background counts are uniformly present in all energy channels but are most obvious in the highest energy channels that normally have the lowest non-background count rates. The intensity of the SEP background count rate increases with time and results in complete whiteout conditions over all energies for the interval Day 309.65 to Day 310.05. During this time, no reliable solar wind measurements, which are important for understanding how energy and mass are coupled into the Earth's space environment and for predicting geomagnetic activity, can be acquired.

Avalanches initiated by penetrating radiation also contribute to the total charge output of CEM and MCP detectors. Because the primary parameter governing detector lifetime is the total

Manuscript received February 19, 2015; revised June 05, 2015; accepted July 30, 2015. Date of publication October 02, 2015; date of current version October 09, 2015. Work at Los Alamos was enabled by the Laboratory Directed Research and Development Program and performed under the auspices of the U.S. Department of Energy .

H. O. Funsten is with the Intelligence and Space Research Division, Los Alamos National Laboratory, Los Alamos, NM 87545 USA (e-mail: hfunsten@lanl.gov).

R. W. Harper, B. A. Larsen, and R. M. Skoug are with the Space Science and Applications Group, Los Alamos National Laboratory, Los Alamos, NM 87545 USA (e-mail: rharper@lanl.gov; balarsen@lanl.gov; rskoug@lanl.gov).

E. E. Dors is with the Emerging Threats Program Office, Los Alamos National Laboratory, Los Alamos, NM 87545 USA (e-mail: edors@lanl.gov).

P. H. Janzen is with the Department of Physics and Astronomy, University of Montana, Missoula, MT 59812 USA (e-mail: paul.janzen@umontana.edu).

E. A. MacDonald is with the Sciences and Exploration Directorate, Goddard Space Flight Center, Greenbelt, MD 20771 USA (e-mail: elizabeth.a.macdonald@nasa.gov).

D. I. Poston is with the Systems Design and Analysis Group, Los Alamos National Laboratory, Los Alamos, NM 87545 USA (e-mail: poston@lanl.gov).

S. M. Ritzau is with Photonis USA Inc., Sturbridge, MA 01566 USA (e-mail: S.Ritzau@usa.photonis.com).

T. H. Zurbuchen is with the Department of Atmospheric, Oceanic, and Space Sciences, University of Michigan, Ann Arbor, MI 48109 USA (e-mail: thomasz@umich.edu).

Color versions of one or more of the figures in this paper are available online at http://ieeexplore.ieee.org.

Digital Object Identifier 10.1109/TNS.2015.2464174

[1]For reference, the CSDA ranges of 10 MeV electrons and 100 MeV protons in aluminum are 2.2 cm and 3.7 cm, respectively [10].

0018-9499 © 2015 IEEE. Translations and content mining are permitted for academic research only. Personal use is also permitted, but republication/redistribution requires IEEE permission. See http://www.ieee.org/publications_standards/publications/rights/index.html for more information.

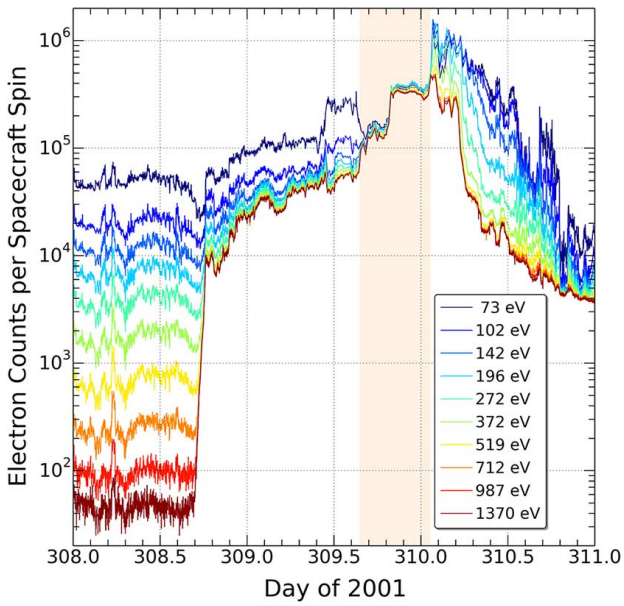

Fig. 1. An example of background counts from penetrating radiation in space: the ACE/SWEPAM solar wind plasma spectrometer experiences white-out conditions during passage of a solar energetic particle (SEP) event. Shown are the total counts per spacecraft spin from the SWEPAM CEM detectors in electron detection mode. The SEP event starts at $\sim$ 308.7, when background counts from the penetrating radiation far exceed counts from solar wind electrons in the higher energy channels, which typically see the fewest solar wind electrons. All energy channels experience complete white-out conditions from background counts due to penetrating radiation from Day 309.65 to Day 310.05 (tan shaded area).

charge output [1], [12]–[14], penetrating radiation can shorten CEM and MCP detector lifetime. Thus, detectors that are sensitive to penetrating radiation can experience both high background count rates and a shortened lifetime.

Techniques for mitigation of background counts from penetrating radiation are generally limited. Shielding is an obvious method but requires substantial mass resources that come at tremendous launch cost and can serve as a conversion medium to create many low energy secondary particles (to which CEM and MCP detectors are sensitive) from one incoming high-energy particle. Another mitigation strategy is to focus the incident particles to a smaller area so that a smaller detector can be employed. Another technique is to surround the CEM or MCP detector with an anticoincidence shield [15] for rejection of some types of penetrating radiation, although this results in additional complexity as well as mass and power resources, and high event rates of the anticoincidence detector can paralyze an instrument. Finally, for measurement of some species such as ions and energetic neutral atoms, coincidence or time-of-flight measurements can be used for identification of signal counts in the presence of substantial background counts [5], [7].

CEM and MCP detectors are largely interchangeable for simple detection of individual particles, although MCP detectors are often utilized for applications requiring position sensing, fast timing, and large detection area. However, recent developments of multiple-channel CEM detectors has enabled their use in fast-timing applications, such as the Photonis MAGNUM detector with a 1.7 ns pulse width. The purpose of this study is to understand the relative sensitivity of MCP and CEM detectors to background counts from penetrating radiation. While our primary application is penetrating radiation in the space environment, these results can apply to any penetrating radiation whose endpoint energy cascade is predominantly low energy electrons, which we call "cascade" electrons, that mimic the photoelectrons or secondary electrons that these detectors are optimized to detect.

We hypothesize that, compared to CEM detectors, MCP detectors have a substantially larger internal surface area that is sensitive to cascade electrons from penetrating particles. We measure the relative detection efficiencies of MCP and CEM detectors to γ-rays, which are a reasonable and general proxy for background counts in CEM and MCP detectors induced by penetrating radiation. While detailed models of the interaction of hard x-rays and γ-rays in MCP detectors have been developed [16], [17], the relative responses of CEM and MCP to γ-rays have not been characterized.

γ-rays interact with solids through three dominant processes: photoelectric absorption, Compton scattering, and pair production. For the 662 keV γ-rays used in this study, pair production is negligible, and both photoelectric absorption and Compton scattering evolve to a low energy electron shower in the material. Thus, we can apply the results obtained here with 662 keV γ-rays to other types of penetrating radiation (i) that weakly interact with the detector material and (ii) whose interactions are predominantly electronic with an energy endpoint that includes low energy secondary- or photo-electrons, to which electron multipliers are particularly sensitive. In addition to γ-rays, this includes neutrons, cosmic rays, and relativistic ions (greater than $\sim$ 100 MeV/nucleon) and electrons (greater than $\sim$ 10 MeV). 662 keV γ-rays thus serve as an adequate proxy for these types of penetrating radiation.

A. CEMs and MCPs: Continuous Dynode Multipliers

Fig. 2 shows schematically the principle of operation of (a) MCP and (b) CEM detectors. An MCP detector uses two (chevron configuration) or three (z-stack configuration) stacked microchannel plates. Typically, each microchannel plate is $\sim$ 1 mm thick with a vast array of hollow channels, typically with a diameter of $2-10$ μm. A voltage applied across the plates generates an electric field along the channels. An incident particle strikes the entrance surface or a channel wall and generates a secondary electron or photoelectron. This electron is accelerated down the channel, generating sequentially more electrons if the electric field is sufficiently high. The avalanche exits the channel and is collected on the anode as an electron pulse of $10^6 - 10^8$ electrons [17], which can be quickly processed by standard electronics.

The gain G of an avalanche in a channel can be generally described by $G = Y_0 Y^{L/d}$[19]–[23] where Y_0 is the initial secondary electron or photoelectron yield from the interaction of the incident radiation with the detector, Y is the mean secondary electron yield when an avalanche electron strikes the channel wall, L is the channel distance over which an avalanche multiplication occurs, and d is the average distance an electron in the avalanche travels before it impacts a wall and generates one or more secondary electrons that further contribute

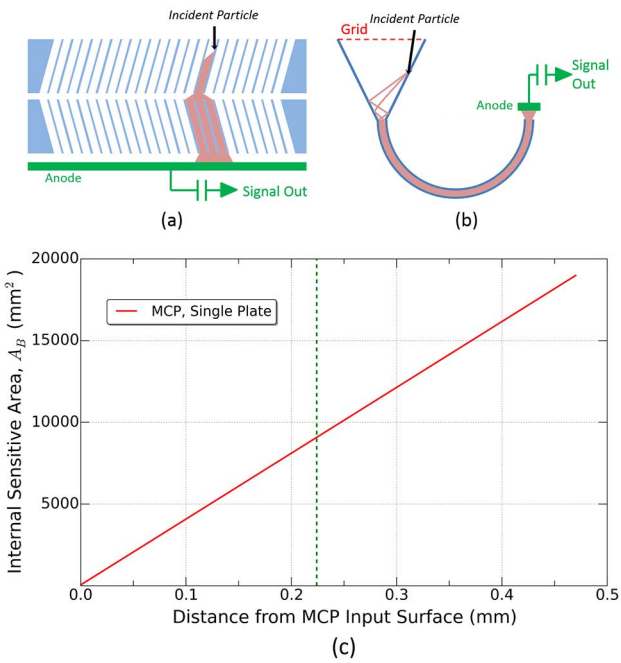

Fig. 2. Schematic illustration of (a) MCP and (b) CEM detectors. MCP detectors have a high density of channels, whereas CEM detectors typically have a funnel and single multiplication channel. The pink shows electron avalanches propagating through the electron multiplication channel(s) to the anode. The total internal area A_B that is sensitive to initiation of an electron avalanche by penetrating radiation is shown for a single microchannel plate in (c) as a function of distance from the input surface of the plate, assuming the same input area (160 mm^2) as the CEM detector. The vertical green dashed line in (c) corresponds to the distance 0.22 mm at which the sensitive area equals 20 times the 455 mm^2 sensitive area of the CEM funnel.

to the avalanche. Equivalently, L/d roughly corresponds to the number of stages in a discrete dynode multiplier.

The CEM detector operates by a similar principle. An incident particle strikes the entrance funnel, generating secondary or photoelectrons that are accelerated into a multiplication channel by the electric field. Electron multiplication occurs throughout this channel, and the avalanche exits onto an anode. Although the ratio L/d, and thus the gain, of a CEM funnel is substantially smaller than that of the CEM channel, it has a much larger surface area that is sensitive to avalanche initiation by penetrating radiation.

Except for specialized applications, e.g. [24], MCPs and CEMs are designed to detect particles that generate secondary electrons or photoelectrons at or near the entrance surface of the detector, such that an electron avalanche is initiated near the input surface. In general, such particles do not penetrate deeply into the detector, and the electron avalanche is amplified through the entire multiplication length of the device.

B. Susceptibility to Penetrating Radiation

Penetrating radiation can generate background counts in MCP and CEM detectors in two ways: (i) by direct interaction with the detectors and emission of low energy electrons from detector surfaces, and (ii) by interaction with nearby components and emission of low energy secondary electrons from component surfaces that can subsequently be detected. This second pathway is typically mitigated by applying a negative bias (e.g., -100 V) to the detector input surface relative to the potential of nearby component surfaces. We therefore only consider the first pathway for background in which penetrating radiation directly interacts with the detector and generates low energy electron emission from detector surfaces.

An important difference between CEM and MCP detectors is the total *internal* surface area A_B that can generate a background count from cascade electrons generated by a penetrating particle. The background count rate is

$$C_B = A_B \phi_B P_B. \tag{1}$$

where A_B is the total sensitive area of the detector that can generate an avalanche with sufficient gain to register a valid pulse and P_B is probability of avalanche initiation by penetrating radiation. In space, the penetrating radiation flux can be omnidirectional; for simplicity, and consistent with the geometry of the experiment used for this study, ϕ_B is defined as an areal flux of incident penetrating radiation (e.g., particles $\cdot$ cm^{-2} $\cdot$ s^{-1}).

The sensitive area of the CEM detector is dominated by its input funnel (455 mm^2), which is nearly $\sim$ 3 times that of the multiplication channel (157 mm^2). In contrast, the sensitive area of an MCP detector is dominated by the surface area of its multiplication channels.

Fig. 2(c) shows the total internal sensitive area A_B of a single microchannel plate as a function of distance into the detector from its input surface. This was calculated for a 160 mm^2 input surface area, which is identical to the CEM detector, and used the same channel diameter (10 μm), channel pitch P (12 μm), and channel length-to-diameter ratio (46/1) as the MCP detector in the experiment. The web comprises 59 mm^2 (37%) of the 160 mm^2 input surface area; this is negligible compared to the sensitive area of the multiplication channels but is included in the calculation.

In contrast to the CEM detector, the sensitive area of the microchannel plate is dominated by the dense array of multiplication channels whose cumulative surface area far exceeds that of the CEM detector. For reference, the green line in Fig. 2(c) shows the distance (0.22 mm) at which the sensitive area of the microchannel plate equals 20 times the sensitive area (455 mm^2) of the CEM funnel.

II. Apparatus and Method

A. CEM Detector

The CEM detector used in this study is a Sjuts model KBL CAS820 with a 0.8 cm $\times$ 2.0 cm rectangular funnel entrance and 15 mm funnel depth. The detector bias V_{CEM} is defined between the front (input) of the CEM and the anode. During exposure to 10 keV H^+, the detector input surfaces of the CEM and MCP detectors were biased to -100 V to prevent detection of spurious secondary electrons that are generated at beam apertures. During exposure to γ-rays, higher energy photoelectrons (e.g., Compton electrons) generated from the interaction of γ-rays with the vacuum chamber walls were blocked from entering into the detector by affixing a 3.18-mm-thick aluminum absorber plate to the border around the CEM funnel.

A 93.1 line-per-inch Ni grid with transmission of 0.88 was placed over the CEM entrance as a fixed equipotential surface to ensure capture of secondary electrons generated in the funnel. A 10 MΩ resistor was placed between the back of the CEM, whose resistance was $\sim$ 180 MΩ, and the anode. The background count rate in the CEM detector with no source present was $< 6 \times 10^{-4}$cts s^{-1}, which is negligible compared to the count rates of $\sim$ 10 cts s^{-1} in the presence of the ^{137} Cs source or when bombarded with 10 keV protons. During exposure to the ^{137} Cs source, the center of the funnel entrance was located 9.8 cm from the source.

B. MCP Detector

The MCP detector used for this study is from a Quantar Technologies Series 3300 detector with a 4.0 cm active diameter with three MCP plates in a z-stack configuration. Similarly to the CEM detector, the MCP bias V_{MCP} is defined between the front (input) surface of the detector and the anode. Each plate had the following properties: 10 μm channel diameter d, 12 μm channel pitch P (center-to-center channel spacing), a channel density of $\sim$ 8000 channels per mm^2, a channel length-to-diameter ratio L/d of 46/1, and a resistance of $\sim$ 30 MΩ. A 9.3 MΩ resistor was placed between the back of the MCP z-stack and the anode, and the MCP signal was extracted from the anode using a high voltage coupling capacitor. The center of the entrance surface of the MCP detector was placed 19.8 cm from the ^{137}Cs source.

The input surface of the MCP detector was biased to -100 V to reject the secondary electrons or photoelectrons generated at vacuum chamber walls. In this configuration, secondary electrons or photoelectrons generated within the web region of the MCP input surface are electrostatically repelled from the MCP and not counted [25]. During γ-ray irradiation, higher energy photoelectrons (e.g., Compton electrons) generated from the interaction of γ-rays with the vacuum chamber walls were blocked from the detector by a 3.18-mm-thick aluminum absorber plate that covered the field-of-view of the detector. Because the MCP detector assembly prevented placement of the absorber place directly on the MCP input surface, the absorber plate was placed $\sim$ 10 cm from the MCP input surface and biased to ground potential.

In contrast to the CEM detector, we find a significant quiescent background count rate in the MCP detector. Fig. 3 shows the output MCP pulse height distribution (PHD) as a function of applied voltage V_{MCP} in a quiescent state with no incident radiation. As V_{MCP} increases, both the total detected counts and the magnitude of the detected pulses increase.

At each value of V_{MCP} shown in Fig. 3, the PHD decreases exponentially with increasing pulse magnitude. Also shown are normalized PHDs for MCP detectors in z-stack configuration operated under quiescent conditions [24], [27] that exhibit the identical behavior of negative exponential PHDs. Background counts in MCP detectors operated under quiescent conditions have been attributed to detection of decay of trace radioactive species in the MCP materials, e.g, from ^{40}K found in the MCPs [27] that uniformly initiate avalanches throughout the multiplication channels in the MCP detector.

A single MCP typically exhibits a negative exponential PHD [18], [28] that can be explained by modeling the statistical evolution of an electron avalanche using a Polya distribution [29]–[31]. However, for the case of a detector in a Chevron or z-stack configuration operated at sufficient bias to induce space charge saturation, incident particles that generate an avalanche in the first MCP generate a strongly peaked, quasi-Gaussian PHD [18], [26]. The negative exponential PHD as observed in Fig. 3 is therefore indicative of uniform avalanche initiation throughout a z-stack MCP detector.

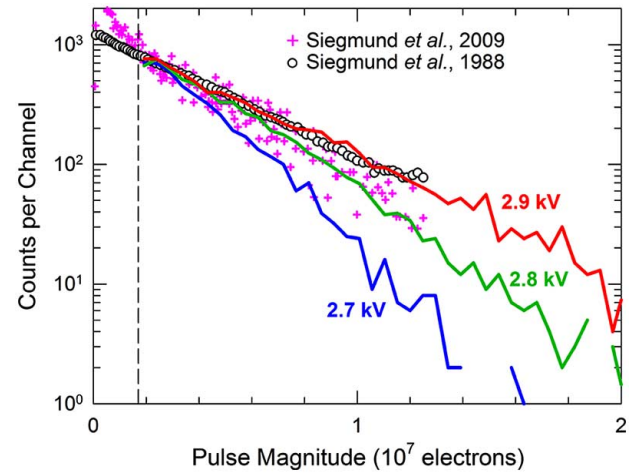

Fig. 3. The MCP pulse height distributions (PHDs) of the quiescent count rate (in the absence of the ^{137}Cs source or incident ions) are shown for three detector biases V_{MCP} for a z-stack configuration. Each PHD was acquired over 1000 s, with average count rates ranging from 4.4 cts $\cdot$ s^{-1} at $V_{\mathrm{MCP}} = 2.7$ kV to 7.4 cts$\cdot\mathrm{s}^{-1}$ at 2.9 kV. Also shown are quiescent MCP pulse height spectra from z-stack detectors [24], [27] that have been normalized to span a pulse magnitude range up to 1.25×10^7 electrons and overlap the data of this study at the LLD setting of 1.7×10^6 electrons (dashed vertical line).

C. PHD Electronics

Electronics for CEM and MCP detectors operated in pulse counting mode are typically optimized for output pulse magnitudes within a particular range (e.g., $10^6 - 10^8$ electrons) appropriate for the detector and the particle targeted for measurement; here, our targeted particle is 10 keV H^+. The outputs of the CEM and MCP detectors were input into a charge-to-voltage converting preamplifier, followed by a shaping (voltage) amplifier, whose output was then measured using a pulse height analyzer. For all experiments of this paper, the lower level discriminator setting Q_{LLD} was fixed such that no counts with charge less than $Q_{\mathrm{LLD}} = 1.7 \times 10^6$ electrons are detected.

D. 10 keV H^+ as Input Radiation

H^+ is ubiquitous in the space environment and is a primary measurement target for understanding the bulk physical properties of space plasmas, whether by *in situ* measurement of H^+ or by remote sensing enabled by energetic neutral atom imaging [6], [32]. Plasma instrumentation, and thus CEM and MCP detectors used in these instruments, are routinely optimized for detection of hydrogen at keV energies. We therefore use 10 keV H^+ to identify the optimum CEM and MCP biases for such a measurement, and then compare the detector responses at the same detector biases to penetrating radiation using

662 keV γ-rays as a proxy. The 10 keV H^+ beam was generated in the Los Alamos Space Plasma Instrument Calibration Facility (see Appendix of [5]).

10 keV H^+ does not penetrate deeply into the detectors and deposits all of its energy near the detector input surface. Based on Stopping and Range of Ions in Matter (SRIM) calculations [33], the mean range of 10 keV H^+ in PbO, which is a reasonable representation of the composition of the channel surface material in CEM and MCP detectors, is 0.13 μm assuming a PbO density of 5 g cm^{-3}. Therefore, incident H^+ deposits all of its energy and generates secondary electrons close to the location at which it impacts the detector material.

E. ^{137}Cs *γ-ray Source*

A ^{137}Cs source was selected for this study because its 662 keV γ-rays are sufficiently energetic to easily penetrate the detectors; with only a few percent attenuation in the detectors, they uniformly illuminate the volume of the detector and generate cascade electrons throughout the length of the multiplication channels. 94.6% of the ^{137}Cs nuclear decay is through internal conversion, with β decay (electron energy between 0 and 518 keV) to metastable $^{137\,m}$Ba, followed by transition to ground state ^{137}Ba via emission of a 662 keV γ-ray. The remaining 5.4% of the ^{137}Cs nuclear decay is transition directly to the ^{137}Ba ground state through 1.18 MeV β-decay electron emission. The source had an activity of 59.2 μCi (2.2×10^6 Bq).

The β-decay electrons are more rapidly absorbed than the γ-rays and therefore deposit their energy closer to the input surface of the detectors. With the goal of maximizing the γ-ray flux and minimizing the electron flux from β emission to fully emulate a uniform energy deposition by penetrating radiation throughout the detector, we placed an aluminum plate in front of and in contact with the ^{137}Cs source to attenuate the electrons. For reference, the electron range in aluminum is $\sim$ 2.6 mm at 1.2 MeV [34], so we selected an aluminum absorber plate thickness of 3.18-mm-thick that was 20% thicker than this range.

Initial experiments showed a significant contribution to measured counts in both CEM and MCP detectors from Compton electrons that are generated by γ-ray interactions with the vacuum chamber walls and the ^{137}Cs mounting assembly. This background was larger in the MCP detector due to its larger input surface area compared to the CEM detector. A second aluminum absorber plate, also 3.18-mm-thick, was subsequently placed immediately in front of the MCP and CEM detectors and covered their entire input surfaces, as previously discussed. The Compton edge for 662 keV γ-rays is 477 keV, so Compton electrons from chamber walls are completely stopped in this second absorber.

We simulated the performance of the absorber plates using Geant4 [35], [36]. The simulations used a ^{137}Cs point source and a single 6.4-mm-thick aluminum absorber plate. The simulation tracked β-decay electrons and γ-rays from the ^{137}Cs source as well as Compton electrons generated in the absorber plate. The simulation results indicate that (a) the absorber plate blocks 100% of the β-decay electrons, (b) 88.0% of the 662 keV γ-rays are transmitted through the absorber plate, and (c) the Compton electron flux exiting the absorber plate is 0.25% of the exiting γ-ray flux.

TABLE I
^{137}Cs 662 keV γ-RAY RATE AT THE DETECTOR INPUT SURFACE

Source-Detector Distance [cm]	Detector	Detector Area [cm^2]	Detector Solid Angle [sr]	γ-ray Rate at Detector Input, R_γ [s^{-1}]
19.0	MCP	12.6	0.0345	5021
9.8	CEM	1.6	0.0167	2423

Using these simulation results and the distances between the ^{137}Cs source and detector input surfaces listed in Table I, we calculated the average γ-ray flux and derived the total incident γ-ray rates R_γ at the CEM and MCP detector input surfaces. The results are listed in Table I.

III. RESULTS AND DISCUSSION

A. PHD from Incident 10 *keV* H^+

Fig. 4 shows the PHDs of the (a) CEM detector and (b) MCP detector resulting from the incident 10 keV H^+ beam. All distributions are strongly peaked, which is characteristic of incident radiation that initiates an electron avalanche near the input surface of the detector, and the avalanche is amplified over nearly the full length of the multiplication channels of the CEM and MCP detectors.

The absolute peak locations and widths of the pulse height distributions are governed by the statistics of electron emission as well as the detailed geometry, material, and avalanche evolution statistics of the electron multiplier. However, we both expect [19]–[21], [26] and observe an increase in both the PHD peak location (mean gain) and peak width (gain dispersion) of the MCP and CEM detectors with increasing detector bias.

As previously stated, electronics used for electron multiplier counting are optimized for a specific range of pulse magnitudes. Each PHD in Fig. 4(a) is matched to a similar PHD in Fig. 4(b) according to line color. This allows comparison of the γ-ray responses of these detectors while operating at detector biases that give similar gain performance for detection of 10 keV H^+.

As discussed later, the detector bias for detection of 10 keV H^+ in space is set so that the peak of the pulse height distribution lies sufficiently above the lower level discriminator setting so that almost all H^+ events register a valid pulse. In this configuration, most or all incident H^+ that generate avalanches are detected. In Fig. 4, this corresponds to approximately $V_{\mathrm{CEM}} \geq 2.1$ kV and $V_{\mathrm{MCP}} \geq 2.9$ kV. A detector bias significantly higher than these values provides higher gain; however, this additional gain (1) provides no or minimal increase in quantum detection efficiency of H^+, (2) reduces detector lifetime, which correlates with total charge output [1], [12]–[14], and (3) increases the background count rate from penetrating radiation as discussed in the next two sections.

B. PHD from Incident 662 *keV γ-rays*

Fig. 5 shows the pulse height distributions of the (a) CEM detector and (b) MCP detector during exposure to 662 keV γ-rays under the conditions listed in Table I. The counts are normalized to the γ-ray flux traversing the detector input surfaces, which is

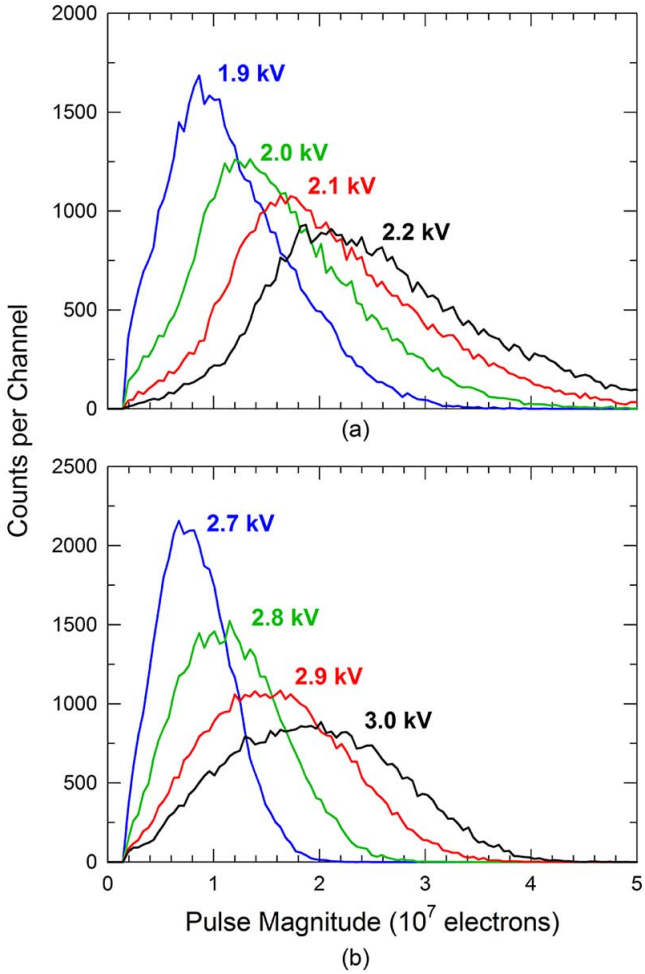

Fig. 4. The pulse height distributions (PHDs)of the (a) CEM and (b) MCP detectors resulting from incident beams of 10 keV H^+ form strongly peaked distributions at all applied detector biases V_{CEM} and V_{MCP}. The similar PHD line colors of (a) and (b) show approximately matched gain performance, which enables comparison of CEM and MCP responses to γ-rays. (a) 10 keV H^+ on CEM Detector (b) 10 keV H^+ on MCP Detector.

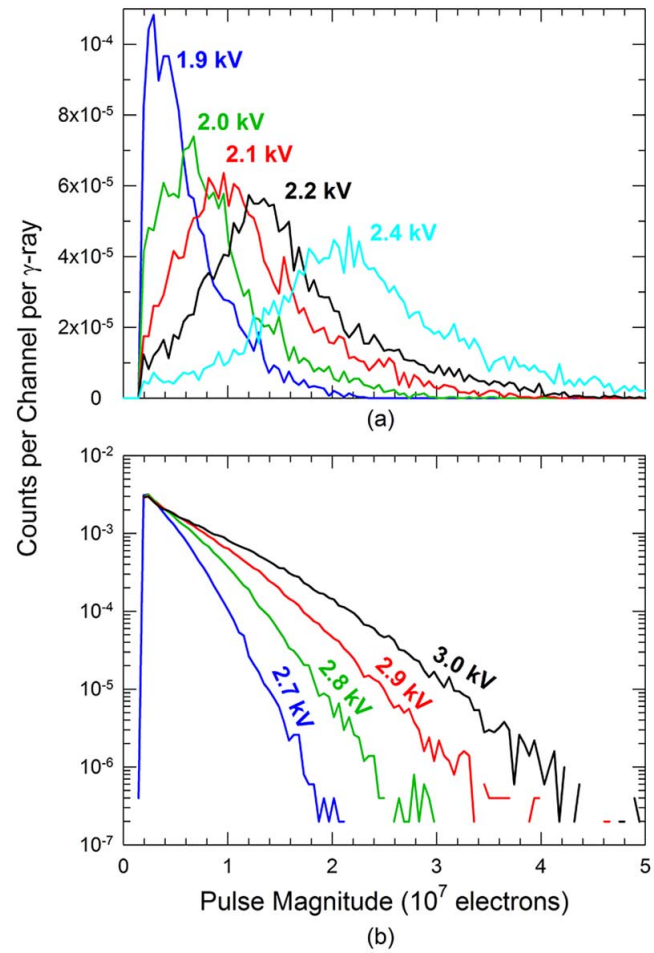

Fig. 5. The pulse height distributions (PHDs) of the (a) CEM and (b) MCP detectors resulting from incident 662 keV γ-rays from ^{137}Cs as a function applied detector bias V_{CEM} and V_{MCP}. At each detector voltage, the PHD was acquired over 1200 s for the CEM detector and 1000 s for the MCP detector. The CEM PHD at $V_{\mathrm{CEM}} = 2.4$ kV is included to clearly show that γ-rays form a strongly peaked PHD in the CEM, similar to 10 keV H^+. (a) 62 keV γ-rays on CEM Detector (b) 622 keV γ-rays on MCP Detector.

also listed in Table I. This allows quantitative comparison of the CEM and MCP detector sensitivities to γ-rays. The similar line colors of the PHDs in Fig. 5(a) and Fig. 5(b) correspond to similar gain performance for detection of 10 keV H^+ as derived in Fig. 4. For example, through similar PHD in Fig 4, the γ-ray sensitivity for the CEM detector at $V_{\mathrm{CEM}} = 2.1$ keV can be directly compared to the MCP γ-ray sensitivity at $V_{\mathrm{MCP}} = 2.9$ keV.

For the CEM detector results shown in Fig. 5(a), a distinct peak is observed in the PHD at each detector voltage V_{CEM}. These peaks are of similar shape to those observed for the incident H^+ beam shown in Fig. 4(a), although the γ-ray PHD peak maxima occur at slightly lower pulse magnitudes in the MCP detector compared to the CEM detector. The lower PHD peak for incident γ-rays is characteristic of a smaller initial secondary electron yield Y_0 of γ-rays relative to 10 keV H^+[19]–[22].

The shape of the γ-ray PHD peak in the CEM detector is consistent with the domination of the sensitive area by the CEM funnel. Because the γ-rays initiate most electron avalanches in the funnel, these avalanches are subsequently fully amplified as they traverse the entire multiplication channel, creating the relatively well-defined peak that is observed that is similar in shape to the PHD from incident H^+.

In contrast, Fig. 5(b) shows the MCP PHD from incident 662 keV γ-rays for the same MCP biases used in Fig. 4(b). At each MCP detector bias, the PHD decreases as a negative exponential distribution, which is consistent with the quiescent, exponentially-decreasing PHD of Fig. 3 that we attribute to uniform avalanche initiation throughout the multiplication channels of the MCP detector. These PHDs contrast sharply with the distinctly peaked PHD from incident γ-rays in the CEM detector (Fig. 5(a)) and from H^+ detection by the MCP detector (Fig. 4(b)).

C. Detection Efficiencies for Incident 662 keV γ-rays

Table II shows average CEM and MCP detector count rates R_{Q} under quiescent conditions with no input radiation, count rates R_{E} during exposure to 662 keV γ-rays, and the net count rates $R_{\mathrm{N}} = R_{\mathrm{E}} - R_{\mathrm{Q}}$ due to the 662 keV γ-rays from the

TABLE II
RESPONSE OF CEM AND MCP DETECTORS TO 662 keV γ-RAYS

	Bias [kV]	Quiescent Rate, R_Q [s^{-1}]	Rate during γ-ray exposure, R_E [s^{-1}]	Net Rate, R_N [s^{-1}]	Quantum Efficiency, ε_γ
CEM Detector	1.9	<10^{-3}	3.33	3.33	0.00137
	2.0	<10^{-3}	3.53	3.53	0.00146
	2.1	<10^{-3}	4.13	4.13	0.00170
	2.2	<10^{-3}	4.23	4.23	0.00175
	2.3	<10^{-3}	4.36	4.36	0.00180
	2.4	<10^{-3}	4.25	4.25	0.00175
MCP Detector	2.7	3.14	110.1	105.7	0.02104
	2.8	4.44	144.3	138.4	0.02757
	2.9	5.92	174.2	166.8	0.03322
	3.0	7.39	202.6	193.7	0.03858

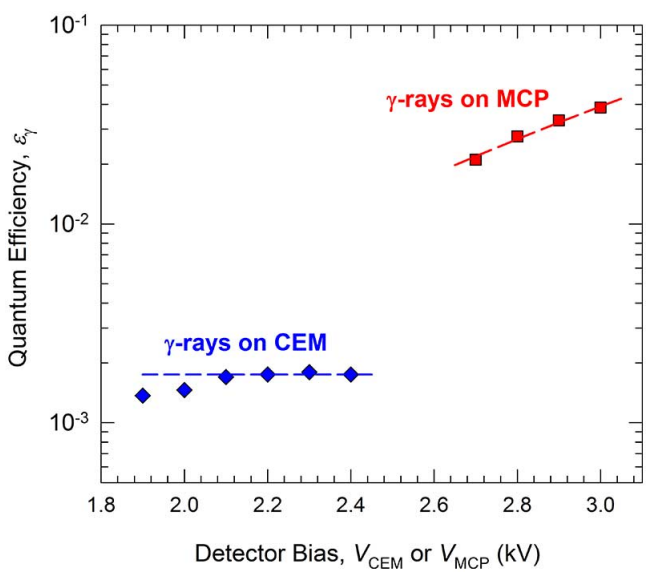

Fig. 6. The quantum efficiency ε_γ for detection of 662 keV γ-rays for the CEM detector (blue diamonds) and MCP detector (red squares) are shown as a function of detector bias. The dashed red line is a power law fit to data, $\varepsilon_\gamma = 9.5 \times 10^{-5}(V_{\rm MCP})^{5.5}$, showing a strong dependence on detector bias. In contrast, the quantum efficiency of the CEM detector is a constant $\varepsilon_\gamma = 1.75 \times 10^{-3}$ when the strongly peaked γ-ray PHD lies above the LLD, which corresponds to $V_{\rm CEM}$ in the range 2.1-2.4 kV; the dashed blue line is the average ε_γ at these biases.

^{137}Cs source. The quiescent count rates R_Q for the CEM detector are negligible in comparison to the total count rates measured during γ-ray exposure.

Also listed in Table II is the quantum efficiency ε_γ of the detectors to 662 keV γ-rays. This efficiency is obtained from the ratio of the net detector count rate R_N from these γ-rays listed in Table II to the calculated γ-ray input rate R_γ listed in Table I. The error of ε_γ based on counting statistics is $< 0.5\%$ for the CEM detector and $< 0.3\%$ for the MCP detector.

The quantum efficiency is also shown in Fig. 6 as a function of applied detector bias. For the CEM detector, ε_γ varies little with detector bias $V_{\rm CEM}$, with an average value of 0.00175 for the four highest detector biases. This behavior is expected because the peak of the PHD of Fig. 5(a) is mostly or entirely above the lower level discriminator setting at corresponding voltages. Thus, additional gain resulting from higher detector bias yields no additional counts from γ-rays.

From Table II, the MCP detector has considerably higher quantum detection efficiency ε_γ than the CEM detector. Furthermore, ε_γ increases substantially with increasing detector bias, with ε_γ ranging from 1.06% at $V_{\rm MCP} = 2.6$ kV to 2.5% at 3.0 kV. These results are generally consistent with previous quantum efficiency measurements of $\sim 2\%$ for 662 keV γ-rays [1].

Fig. 6 shows the strong dependence of ε_γ on $V_{\rm MCP}$. The quantum efficiencies are fit to a power law function $\varepsilon_\gamma = a(V_{\rm MCP})^k$, whose scaling exponent k is a quantitative measure of the dependence of ε_γ on $V_{\rm MCP}$. Using the data points at the four highest detector biases (for which the 10 keV H^+ pulse height distributions are completely above the lower level discriminator setting), the power law fit yields $k = 5.5 \pm 0.5$, which is shown as the dashed red line in Fig. 6. This clearly demonstrates a strong, nonlinear dependence of ε_γ on $V_{\rm MCP}$.

Using a constant value $\varepsilon_\gamma = 0.00175$ for the CEM detector, the ratio $(\varepsilon_\gamma)_{\rm MCP}/(\varepsilon_\gamma)_{\rm CEM}$ of the MCP and CEM quantum efficiencies for detection of 662 keV γ-rays equals 18 at $V_{\rm MCP} = 2.9$ kV and 22 at $V_{\rm MCP} = 3.0$, yielding an average value $(\varepsilon_\gamma)_{\rm MCP}/(\varepsilon_\gamma)_{\rm CEM} \approx 20$. From the green line of Fig. 2(c), a ratio of the MCP-to-CEM sensitive surface area corresponding to 20 is obtained when all avalanches generated within 0.22 mm of the input surface of the first microchannel plate of the z-stack MCP detector register valid pulses.

To confirm that 662 keV γ-rays uniformly penetrate the CEM detector, we compared the CEM response to γ-rays under two conditions: with the CEM detector input surface facing the ^{137}Cs source (identical to the orientation for the data of Fig. 4(b)) and with the CEM rotated 90° so that its longer side dimension faced the source. The ratio of counts obtained in the front relative to side orientations was 0.986 ± 0.017, illustrating the uniform penetration through and uniform energy deposition within the detector. Similar measurements of the MCP detector were not possible due to the significant mass of the MCP detector mounting assembly, although we note that edge-on detection by MCP detectors of penetrating radiation has been both studied [37] and applied to x-ray imaging [38], [39]. Edge-on detection is unique due to greater detector thickness and thus higher absorption of penetrating radiation, although the detector area exposed to incoming penetrating radiation flux is smaller.

The CEM results demonstrate that 662 keV γ-rays are a reasonable proxy for penetrating radiation that deposits energy uniformly in the detector and whose energy endpoint is electronic excitation and ionization in the detector material. This result also applies to penetrating radiation such as neutrons, cosmic rays, and relativistic ions and electrons. Because CEM detectors are a factor of $\sim$ 20 less sensitive to penetrating radiation, we have successfully incorporated CEM detectors into both the IBEX-Hi neutral atom imager [8], which uses multiple coincidence detection to measure the tenuous flux of energetic neutral atoms that enter the detector subsystem at a rate of

$\sim 2-3$ atom$\cdot$s^{-1}, and the HOPE time-of-flight mass spectrometer, which uses time-of-flight measurements to measure ions, their masses, and electrons within the harsh penetrating radiation environment of the Earth's radiation belts [5].

D. MCP Sensitivity to Penetrating Radiation: Dependence on Lower Level Discriminator (LLD) Setting

For the MCP detector, the negative exponential pulse height distributions for incident 662 keV γ-rays depicted in Fig. 5(b) strongly contrasts with the 10 keV H^+ PHD (Fig. 4(b)), which are strongly peaked and have a larger average pulse magnitude. This suggests that MCP detector background from penetrating radiation might be substantially reduced relative to a target species such as 10 keV H^+ by increasing the lower level discriminator (LLD) setting $Q_{\rm LLD}$ (or, equivalently, a decrease in detector voltage as indicated in Fig. 6) without significant reduction of target particle counts.

Using the MCP detector PHD data of Figs. 4(b) and 5(b) at $V_{\rm MCP} = 3.0$ kV, Fig. 7(a) shows the total counts that would be detected as a function of $Q_{\rm LLD}$ if $Q_{\rm LLD}$ was an adjustable parameter instead of being fixed at $Q_{\rm LLD} = 1.7 \times 10^6$ electrons as in Fig. 4 and Fig. 5. As expected, the total counts detected for 662 keV γ-rays decreases more rapidly with increasing $Q_{\rm LLD}$ than for 10 keV H^+. In Fig. 7(a) the symbols represent the LLD setting $Q_{\rm LLD}$ at which 90% ($\triangle$), 75% ($\circ$), and 50% ($\square$) of the total H^+ events with $Q_{\rm LLD} > 1.7 \times 10^6$ electrons are registered as valid counts, with the invalid counts rejected because their pulse magnitudes lie below $Q_{\rm LLD}$. Notably, these LLD settings encroach into the H^+ PHD peak shown in Fig. 4(b).

Fig. 7(b) shows the ratio $R_{\rm SB}$ of the counts from H^+ to the counts from γ-rays as a function of $Q_{\rm LLD}$, where $R_{\rm SB}$ is normalized to unity at $Q_{\rm LLD} = 1.7 \times 10^6$ electrons. $R_{\rm SB}$ is therefore a relative measure of the signal-to-background ratio, and we also note that $R_{\rm SB}$ is proportional to the quantum detection efficiency ratio $\varepsilon_{\rm H+}/\varepsilon_\gamma$.

The opportunity to reduce the penetrating radiation background counts by increasing the LLD setting $Q_{\rm LLD}$ is apparent from Fig. 7(b). Factors of 3, 6, and 12 in signal-to-background can be gained with 10%, 25%, and 50% reductions in valid H^+ counts. While these gains in signal-to-background are enticing and may be practical in some applications, measuring particles such as H^+ with an LLD setting inside its PHD peak can substantially reduce the measurement accuracy. We illustrate this through a gain–voltage curve, which is typically used to set detector bias and monitor performance of CEM and MCP detectors in space.

For space applications, electronics that process output pulses from CEM and MCP detectors are designed and optimized to accept valid pulses over a specified range of output charge magnitudes. This range is needed because of the expected variation of pulse magnitudes due to avalanche statistics and to the secondary electron emission statistics of initial impact of the incident particle, which can vary substantially depending on particle type and energy. Typically, the lower and upper level discriminator settings are fixed, and the CEM or MCP detector gain is optimized by adjusting the detector bias $V_{\rm D}$ in order to match the PHD of the suite of targeted particles and energies to the electronics.

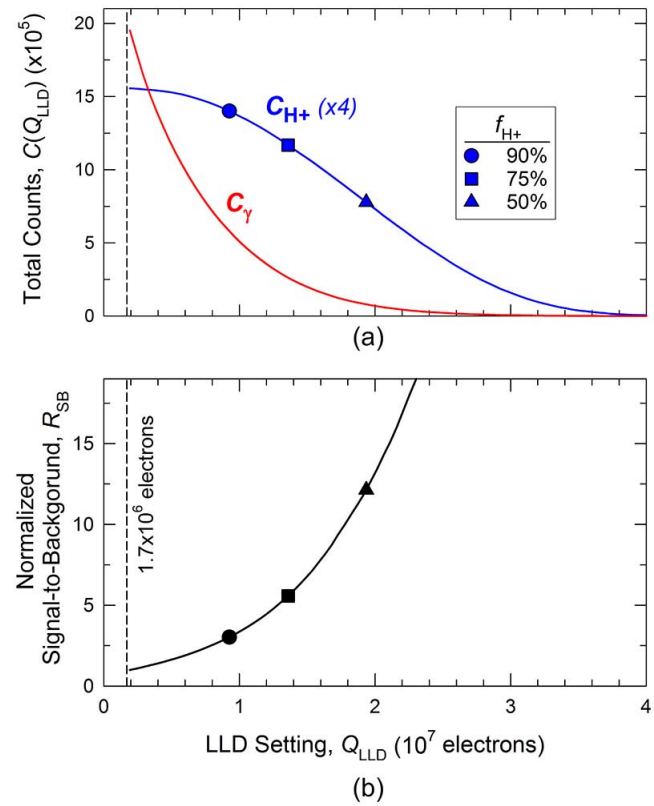

Fig. 7. Adjustment of the lower level discriminator $Q_{\rm LLD}$ can reduce the sensitivity of an MCP detector to penetrating radiation, although at the expense of the detection efficiency of the targeted particles. (a) Using the PHD data of Fig. 5(a) and 5(b), respectively, acquired at $V_{\rm MCP} = 3.0$ kV, the total counts registered in the MCP detector for incident 10 keV H^+ and (blue line) 662 keV γ-rays (red line) are shown as a function of lower level discriminator setting $Q_{\rm LLD}$. The H^+ counts have been multiplied by a factor of 4 for easy comparison with the counts from γ-rays. As $Q_{\rm LLD}$ increases, fewer valid counts are registered, and the fraction of counts above $Q_{\rm LLD}$ decreases faster for γ-rays than for H^+. (b) The signal-to-background ratio $R_{\rm SB}(Q_{\rm LLD}) \propto C_{\rm H+}(Q_{\rm LLD})/C_\gamma(Q_{\rm LLD})$, which is normalized to unity at $Q_{\rm LLD} = 1.7 \times 10^6$ electrons, increases with increasing $Q_{\rm LLD}$, illustrating a method for potential improvement in signal-to-background ratio. The symbols in (a) and (b) are shown at the LLD settings at which the relative fractions $f_{\rm H+}(Q_{\rm LLD})$ of valid H^+ counts equal 50% ($\triangle$), 75% ($\square$), and 90% ($\circ$), where $f_{\rm H+}(Q_{\rm LLD}) = C_{\rm H+}(Q_{\rm LLD})/C_{\rm H+}(1.7 \times 10^6$ electrons).

A gain-voltage curve is obtained by measuring counts C as a function of detector bias $V_{\rm D}$ for a constant input particle flux. Fig. 8 shows for illustrative purposes an MCP detector gain-voltage curve from a constant-flux 10 keV H^+ beam. The normalized gain-voltage curve, which is proportional to quantum detection efficiency, is well-represented by a Logistic function

$$\frac{C\left(V_D\right)}{C_{MAX}} = \frac{1}{1 + \exp\left(-\left(V_D - V_M\right)/V_{\rm W}\right)} \tag{2}$$

where $C_{\rm MAX}$ is the maximum count rate, $V_{\rm M}$ is the detector bias at the midpoint of the curve (i.e., where $C(V_D)/C_{\rm MAX} = 0.5$), and $V_{\rm W}$ is a width parameter that is a measure of the steepness of the gain-voltage curve. Also shown in Fig. 8 is the derivative of Eq. (2) (green line), which illustrates the relative steepness of the gain-voltage curve as a function of detector bias.

Typically, the nominal operating detector bias is set to

$$V_0 \geq V_{\rm M} + 5V_{\rm W}, \tag{3}$$

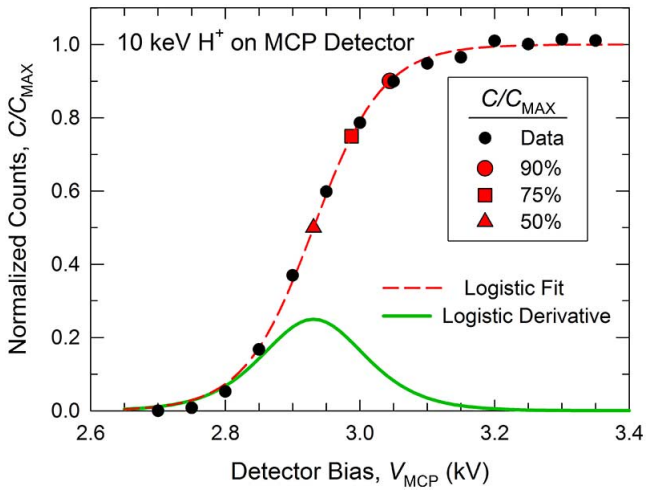

Fig. 8. A typical MCP detector gain-voltage curve (counts as a function of detector bias at a fixed lower level discriminator setting) is shown for incident 10 keV H^+ (black points). The gain-voltage curve is well-represented by a Logistic function (red line). For direct comparison with Fig. 7, the red symbols indicate the detector bias at which 50% (△), 75% (□), and 90% (○) of the H^+ counts are registered as valid counts. The green curve shows the derivative of the logistic function fit; the magnitude of the derivative corresponds to the gain uncertainty for electron multiplier detectors in space.

which allows sufficient gain margin so that most events generated by targeted particles are registered as valid events. In Fig. 8, the fit of the Logistic function to the data yields $V_{\mathrm{M}} = 2.93$ kV and $V_{\mathrm{W}} = 0.052$ (red dashed line), which yields a nominal detector bias of $V_0 \geq 3.2$ kV.

Also shown in Fig. 8 (red points) for direct comparison with Fig. 7 are the detector biases at which 50%, 75%, and 90% of the counts C_{MAX} acquired at nominal bias $V_0 \approx 3.2$ kV are accepted as valid counts. As indicated by the derivative of the Logistic function (green line), these points fall along the generally steep section of the gain-voltage curve. At these points, a small shift in detector gain can result in a large change of C/C_{MAX} and thus of quantum detection efficiency, which degrades the accuracy and precision of the measurements.

The strong dependence of H^+ quantum detection efficiency on gain when operating the detector along the steep section of the gain-voltage curve (e.g., $V_{\mathrm{D}} < 3.1$ kV) has three important consequences for space applications. First, the widths and peak locations of the PHD of targeted particles are dependent on particle properties; equivalently, particles of different type and energy can have slightly different gain-voltage curves. Therefore, operating with a detector bias V_{D} in the steep part of the gain-voltage curve for one particle type and energy intersects the gain-voltage curves of the other particle types and energies at different locations, introducing substantial uncertainty in the relative quantum detection efficiencies of the different particle types and energies.

Second, aging of an MCP detector results in decreasing gain at a rate that primarily depends on the total charge output over its lifetime [40]. From Fig. 8, a slight decrease in gain in the steep part of the gain-voltage curve can result in a significant decrease in quantum detection efficiency. Without precise calibration and knowledge of the gain-voltage curve, both the accuracy of the measurement and its uncertainty are degraded. We note that new lifetime-extension technologies have been developed for MCP photomultiplier (PMT) detectors [41].

Third, in space applications, a gain-voltage curve is periodically acquired to monitor detector performance and aging, and an observed decrease in detector gain is compensated by increasing the detector bias. An important assumption for acquiring a well-calibrated gain-voltage curve is a uniform incident particle flux over the duration of the gain-voltage curve measurement. Unfortunately, incident particle fluxes in space vary substantially over time, resulting in a poorly quantified gain-voltage curve. Using such a gain-voltage curve as a quantitative calibration for operating the MCP detector in the steep section of the gain-voltage curve introduces substantial uncertainty in the measurements.

With these considerations, increasing the signal-to-background by increasing the LLD setting is generally not practical for space applications unless lower measurement accuracy is acceptable or an *in situ* method for regular, accurate gain-voltage curve calibration is implemented for the different targeted particle types and energies.

E. MCP Sensitivity to Penetrating Radiation: Dependence on Detector Geometry

For this analysis, we assume that the incident particles that we are trying to measure can hit the web area of the MCP input surface and be detected. Therefore, the detection efficiency of these particles is largely insensitive to the open area ratio of the detector.

The quantum efficiency of MCP detectors from incident penetrating radiation scales as $\varepsilon_\gamma \propto \rho_{\mathrm{C}} A_{\mathrm{C}}$ where ρ_{C} is the areal channel density and A_{C} is the channel surface area. First, the channel density is inversely proportional to the square of the channel pitch, i.e., $\rho_{\mathrm{C}} \propto P^{-2}$. Second, the channel surface area is $A_{\mathrm{C}} = \pi L d$ where, as before, L and d are the channel length and diameter, respectively. We wish to assess the sensitivity at a specific detector gain; thus, because gain is dependent on the ratio L/d [17]–[20], [26] we likewise require that L/d remains constant for any detector geometry. This results in $A_{\mathrm{C}} \propto d^2$. Therefore, we obtain for MCP detectors

$$\varepsilon_\gamma \propto \left(\frac{d}{P}\right)^2. \tag{4}$$

We note that P/d is a measure of the relative channel wall thickness, thus ε_γ decreases quadratically with increasing relative wall thickness. We further note that the open area ratio (OAR) for hexagonal channel geometry likewise scales as $(d/P)^2$, thus $\varepsilon_\gamma \propto$ OAR.

Using the $\varepsilon_\gamma = 0.0208$ from Table II for the MCP geometry used in this study ($d = 10\ \mu$m, $P = 12\ \mu$m), we can predict the sensitivity of MCP detectors of other geometries using

$$\varepsilon_\gamma = 0.030\left(\frac{d}{P}\right)^2. \tag{5}$$

Therefore, MCP detectors with smaller channel diameter and larger channel pitch results in lower sensitivity to penetrating radiation. Because imaging resolution decreases with larger

channel pitch [42], this optimization is practical for applications that do not require high imaging resolution.

REFERENCES

[1] G. W. Fraser, "X- and γ-ray imaging using microchannel plates," *Nucl. Instrum. Methods Phys. Res. A*, vol. 221, no. 1, pp. 115–130, 1984.

[2] J. G. Timothy, "Microchannel pates for photon detection and imaging in space," in *Observing Photons in Space*, M. C. E. Huber, A. Pauluhn, J. L. Culhane, J. G. Timothy, K. Wilhelm, and A. Zehnder, Eds. New York, NY, USA: Springer, 2010, pp. 365–390 [Online]. Available: http://www.issibern.ch/forads/sr-009-22.pdf, ISSI Scientific Report SR-009

[3] D. J. McComas, S. J. Bame, P. Barker, W. C. Feldman, J. L. Phillips, P. Riley, and J. W. Griffee, "Solar wind electron proton alpha monitor (SWEPAM) for the advanced composition explorer," *Space Sci. Rev.*, vol. 86, no. 1–4, pp. 563–612, 1998 [Online]. Available: http://link.springer.com/article/10.1023%2FA%3A1005040232597#page-1

[4] C. W. Carlson, J. P. McFadden, P. Turin, D. W. Curtis, and A. Magoncelli, "The electron and ion plasma experiment for FAST," *Space Sci. Rev.*, vol. 98, no. 1–2, pp. 33–66, 2001.

[5] H. O. Funsten, R. M. Skoug, A. A. Guthrie, E. A. MacDonald, J. R. Baldonado, R. W. Harper, K. C. Henderson, K. H. Kihara, J. E. Lake, B. A. Larsen, A. D. Puckett, V. J. Vigil, R. H. Friedel, M. G. Henderson, J. T. Niehof, G. D. Reeves, M. F. Thomsen, J. Hanley, D. George, J.-M. Jahn, S. Cortinas, A. De Los Santos, G. Dunn, E. Edlund, M. Ferris, M. Freeman, M. Maple, C. Nunez, T. Taylor, W. Toczynski, C. Urdiales, H. E. Spence, J. Cravens, L. L. Suther, and J. Chen, "Helium, oxygen, proton, and electron (HOPE) mass spectrometer for the radiation belt storm probes mission," *Space Sci. Rev.*, vol. 179, pp. 423–484, 2013 [Online]. Available: http://link.springer.com/article/10.1007%2Fs11214-013-9968-7#page-1

[6] D. J. McComas, B. L. Barraclough, R. C. Elphic, H. O. Funsten, and M. F. Thomsen, "Magnetospheric imaging with low-energy neutral atoms," *Proc. Nat. Acad. Sci.*, vol. 88, no. 21, pp. 9598–9602, Nov. 1991 [Online]. Available: http://www.pnas.org/content/88/21/9598.full.pdf

[7] H. O. Funsten, A. A. Guthrie, R. W. Harper, K. H. Kihara, M. P. Manzo, M. J. Fagan, D. J. McComas, S. Weidner, F. Allegrini, D. Everett, B. Rodriguez, G. Dunn, J. Hanley, M. Maple, K. Mashburn, S. Pope, P. Valek, E. Moebius, J. Nolin, S. Ellis, D. Heirtzler, B. King, H. Kucharek, S. Turco, S. Zaffke, D. Reisenfeld, P. Janzen, S. A. Fuselier, M. Gruntman, E. Roelof, P. Wurz, D. Piazza, L. Saul, and P. Bochsler, "The interstellar boundary explorer high energy (IBEX-Hi) neutral atom imager," *Space Sci. Rev.*, vol. 146, pp. 75–103, 2009 [Online]. Available: http://download.springer.com/static/pdf/303/art%253A10.1007%252Fs11214-009-9504-y.pdf?auth66=1420650164_d44536b65b7de3cd6c3262584ccbaf0a&ext=.pdf

[8] D. J. McComas, F. Allegrini, J. Baldonado, B. Blake, P. C. Brandt, J. Burch, J. Clemmons, W. Crain, D. Delapp, R. DeMajistre, D. Everett, H. Fahr, L. Friesen, H. Funsten, J. Goldstein, M. Gruntman, R. Harbaugh, R. Harper, H. Henkel, C. Holmlund, G. Lay, D. Mabry, D. Mitchell, U. Nass, C. Pollock, S. Pope, M. Reno, S. Ritzau, E. Roelof, E. Scime, M. Sivjee, R. Skoug, T. S. Sotirelis, M. Thomsen, C. Urdiales, P. Valek, K. Viherkanto, S. Weidner, T. Ylikorpi, M. Young, and J. Zoennchen, "The two wide-angle imaging neutral-atom spectrometers (TWINS) NASA mission-of-opportunity," *Space Sci. Rev.*, vol. 142, pp. 157–231, Jan. 2009 [Online]. Available: http://download.springer.com/static/pdf/231/art%253A10.1007%252Fs11214-008-9467-4.pdf?auth66=1420650003_75573536ef1944d67f7b22b7ed333186&ext=.pdf

[9] E. A. MacDonald, M. F. Thomsen, and H. O. Funsten, "Background in channel electron multiplier detectors due to penetrating radiation in space," *IEEE Trans. Nucl. Sci.*, vol. 53, no. 3, pp. 1593–1598, Jun. 2006.

[10] M. J. Berger, J. S. Coursey, M. A. Zucker, and J. Chang, *Stopping-Power and Range Tables for Electrons, Protons, and Helium Ions* [Online]. Available: http://www.nist.gov/pml/data/star/

[11] R. Schwenn, "Space weather: The solar perspective," *Living Rev. Solar Phys.*, vol. 3, no. 2, 2006 [Online]. Available: http://solarphysics.livingreviews.org/Articles/lrsp-2006-2/

[12] A. Egidi, R. Marconer, G. Pizzella, and F. Sperli, "Channeltron fatigue and efficiency for protons and electrons," *Rev. Sci. Instrum.*, vol. 40, no. 1, pp. 88–91, 1969.

[13] W. G. Wolber, B. D. Klettke, and H. K. Lintz, "Comment on channeltron fatigue and efficiency for protons and electrons," *Rev. Sci. Instrum.*, vol. 40, no. 10, pp. 1364–1365, 1969.

[14] B. R. Sandel, A. Lyle Broadfoot, and D. E. Shemansky, "Microchannel plate life tests," *Appl. Opt.*, vol. 16, no. 5, pp. 1435–1437, 1977.

[15] W. B. Feller, P. L. White, P. B. White, O. H. W. Siegmund, A. P. Martin, and J. V. Vallerga, "Microchannel plate special nuclear materials sensor," *Nucl. Instrum. Methods Phys. Res. A*, vol. 652, no. 1, pp. 25–28, 2011.

[16] D. R. Farley, N. Izumi, and O. L. Landen, "Improved modeling of microchannel plate response to hard X-rays," *Nucl. Instrum. Methods Phys. Res. A*, vol. 705, pp. 17–23, 2013.

[17] P. M. Shikhaliev, "Hard X-ray detection model for microchannel plate detectors," *Nucl. Instrum. Methods Phys. Res. A*, vol. 398, no. 2–3, pp. 229–237, 1997.

[18] J. L. Wiza, "Microchannel plate detectors," *Nucl. Instrum. Methods Phys. Res. A*, vol. 162, pp. 587–601, 1979.

[19] E. H. Eberhardt, "Gain model for microchannel plates," *Appl. Opt.*, vol. 18, no. 9, pp. 1418–1423, 1979.

[20] I. P. Csorba, "Current gain parameters of microchannel plates," *Appl. Opt.*, vol. 19, no. 22, pp. 3863–3866, 1980.

[21] E. H. Eberhardt, "An operational model for microchannel plate devices," *IEEE Trans. Nucl. Sci.*, vol. NS-28, no. 1, pp. 712–717, Feb. 1981.

[22] W. E. Baumgartner and W. K. Huber, "Secondary electron emission multipliers as particle detectors," *J. Phys. E, Sci. Instrum.*, vol. 9, no. 5, pp. 321–330, 1976.

[23] H. O. Funsten, R. W. Harper, and D. J. Suszcynsky, "Mean secondary electron yield of avalanche electrons in the channels of a microchannel plate detector," *Rev. Sci. Instrum.*, vol. 67, no. 10, pp. 3478–3482, 1996.

[24] O. H. W. Siegmund, J. V. Vallerga, A. S. Tremsin, and W. B. Feller, "High spatial and temporal resolution neutron imaging with microchannel plate detectors," *IEEE Trans. Nucl. Sci.*, vol. 56, no. 3, pp. 178–182, Jun. 2009.

[25] H. O. Funsten, D. J. Suszcynsky, R. W. Harper, J. E. Nordholt, and B. L. Barraclough, "Effect of local electric fields on microchannel plate detection and spatial resolution," *Rev. Sci. Instrum.*, vol. 67, no. 1, pp. 145–154, 1996.

[26] G. W. Fraser, J. F. Pearson, G. C. Smith, M. Lewis, and M. A. Barstow, "The gain characteristics of microchannel plates for x-ray photon counting," *IEEE Trans Nucl. Sci.*, vol. NS-30, no. 1, pp. 455–460, Feb. 1983.

[27] O. H. W. Siegmund, J. Vallerga, and B. Wargelin, "Background events in microchannel plates," *IEEE Trans. Nucl. Sci.*, vol. NS-35, no. 1, pp. 524–528, Feb. 1988.

[28] E. J. Gamboa, C. M. Huntington, E. C. Harding, and R. P. Drake, "Electronic measurement of microchannel plate pulse height distributions," *Rev. Sci. Instrum.*, vol. 81, no. 10, 2010, Art. No. 10E310.

[29] W. H. Wright, "The detection efficiency of electron multipliers," *Brit. J. Appl. Phys. (J. Phys. D)*, vol. 2, no. 6, pp. 895–901, 1969.

[30] W. S. Anderson, J. C. Armitage, P. Chevreau, J. G. Heinrich, C. Lu, I. McDonald, K. T. McDonald, B. Miller, D. Secrest, and J. Weckel, "Investigations of single-electron avalanches in a proportional drift tube," in *Proc. Symp. Detector Research and Development for the Superconducting Super Collider*, T. Dombeck, V. Kelly, and G. P. Yost, Eds., 1991, pp. 222–224.

[31] A. Biswas and W. H. Farr, Laboratory Characterization and Modeling of a Near-Infrared Enhanced Photomultiplier Tube Jet Propulsion Laboratory, Pasadena, CA, USA, Tech. Rep. JPL-IPN-PR-42-152, Feb. 2003 [Online]. Available: http://ntrs.nasa.gov/archive/nasa/casi.ntrs.nasa.gov/20040191350.pdf

[32] M. A. Gruntman, E. C. Roelof, D. G. Mitchell, H.-J. Fahr, H. O. Funsten, and D. J. McComas, "Energetic neutral atom imaging of the heliospheric boundary region," *J. Geophys. Res.*, vol. 106, no. A8, pp. 15767–15781, Aug. 2001.

[33] J. F. Ziegler, M. D. Ziegler, and J. P. Biersack, "SRIM–The stopping and range of ions in matter (2010)," *Nucl. Instrum. Methods Phys. Res. B*, vol. 268, no. 11–12, pp. 1818–1823, 2010.

[34] "Stopping Powers for Electrons and Positrons," International Commission on Radiation Units and Measurements, Bethesda, MD, USA, ICRU Rep. 37, 1984.

[35] S. Agostinelli, J. Allison, K. Amako, J. Apostolakis, H. Araujo, and P. Arce *et al.*, "GEANT4-a simulation toolkit," *Nucl. Instrum. Methods Phys. Res. A*, vol. 506, no. 3, pp. 250–303, Jul. 2003 [Online]. Available: http://infoscience.epfl.ch/record/49909/files/Ago+03.pdf

[36] J. Allison *et al.*, "Geant4 developments and applications," *IEEE Trans. Nucl. Sci*, vol. 53, no. 1, pp. 270–278, Feb. 2006.

[37] P. M. Shikhaliev, J. L. Ducote, T. Xu, and S. Molloi, "Quantum efficiency of the MCP Detector: Monte Carlo calculation," *IEEE Trans. Nucl. Sci.*, vol. 52, no. 5, pp. 1257–1262, Oct. 2005.

[38] P. M. Shikhaliev and S. Molloi, "Applications of "edge-on" illuminated porous plate detectors for diagnostic X-ray imaging," *Nucl. Instrum. Methods Phys. Res. A*, vol. 487, no. 3, pp. 676–684, 2002.

[39] P. M. Shikhaliev and S. Molloi, "X-ray imaging with "edge-on" microchannel plate detector: First experimental results," *Nucl. Instrum. Methods Phys. Res. A*, vol. 510, no. 3, pp. 401–405, 2003.

[40] J. P. McFadden, D. S. Evans, W. T. Kasprzak, L. H. Brace, D. J. Chornay, A. J. Coates, B. K. Dichter, W. R. Hoegy, E. Holeman, K. Kadinsky-Cade, J. C. Kasper, D. Kataria, L. Kistler, D. Larson, A. J. Lazarus, F. Mozer, T. Mukai, K. W. Ogilvie, G. Paschmann, F. Rich, Y. Saito, J. D. Scudder, J. T. Steinberg, M. Wuest, and P. Wurz, "In-flight instrument calibration and performance verification," *ISSI Sci. Rep. Ser.*, vol. 7, pp. 277–385 [Online]. Available: http://www.issibern.ch/forads/sr-007-04.pdf

[41] A. Lehmann, A. Britting, W. Eyrich, C. Schwar, J. Schwiening, and F. Uhlig, "Significantly improved lifetime of micro-channel plate PMTs," *Nucl. Instrum. Methods Phys. Res. A*, vol. 718, pp. 535–540, 2013.

[42] O. H. W. Siegmund, M. A. Gummin, T. Ravinett, S. R. Jelinsky, and M. Edgar, "Performance of small pore microchannel plates," *Proc. SPIE*, vol. 2808, Oct. 1996.